JKAU: Eng. Sci., **vol. 11 no. 1,** pp. 169-192 (1419 A.H. / 1999 A.D.)

Adaptive Finite-Element Ballooning Analysis of Monopolar Ionized Field

ANWAR MUFTI*, ZAKARIYA AL-HAMOUZ** and MAZEN ABDEL-SALAM**
*Dept. of Electrical and Computer Engineering,
King Abdulaziz University, Jeddah, Saudi Arabia
**Dept. of Electrical Engineering,
King Fahd University of Petroleum & Minerals,
Dhahran, Saudi Arabia

ABSTRACT. This paper presents an adaptive finite-element technique for the analysis of monopolar ionized field in conductor-to-plane configurations without resort to Deutsch's assumption. A new iterative-element ballooning technique is proposed to solve Poisson's equation wherein the commonly used artificial boundary around the transmission line conductor is simulated at infinity. The proposed technique seeks a solution to only one second-order partial differential equation (PDE) rather than a solution to a nonlinear third-order PDE or a solution to two simultaneous second order PDEs as reported in the literature.

The calculated corona current and the ground plane current-density agreed well with those measured experimentally for a laboratory model. Accuracy and simplicity in programming characterize the proposed method.

1. Introduction

High voltage DC has many advantages over conventional AC lines for long distance power transmission. Recently, the economic feasibility of DC transmission has increased with the development of the HV terminal equipment. One of the problems associated with hvdc transmission is the corona occurring on the transmission line conductors and the associated power loss, audible noise, radio interference and television interference.

Many attempts were made to solve the ionized field problem using the finite-element technique (FET)[1-10]. Among all of these attempts, only Abdel-Salam and Al-Hamouz[8,9]

included the ion diffusion in the solution of the describing equations. Other attempts[11,12] included ion diffusion but using other numerical techniques. Ghione and Graglia[11] adopted the finite-boxes technique for the solution of ionized field in conductor-to-plane configurations and wire-duct precipitators. Levin and Hoburg[12] used the donor cell-finite element technique for the solution of the ionized field in wire-duct precipitators.

The efficient finite-element grid generated from quadrangles produced by the intersection of field lines with equipotential contours proposed in[9,10] is used in the present analysis. In order to satisfy the continuity condition and to estimate the discrete space-charges at the grid nodes, the interelectrode spacing was divided into flux-tubes by field lines. The axis of each flux-tube is also a field line along which the grid nodes are located at the intersections with the equipotential contours. Along these flux-tubes, the ions are driven from the coronating conductor to the ground electrode. In comparison with previous approaches for grid generation[5-7], the proposed grid[9,10] makes it easier to formulate the current continuity condition and current density equation along these tubes.

It is well known that the FET calls for bounded region in which the describing equations are to be solved. All attempts reported before[1-5,7-10] assumed fixed artificial boundary around the transmission line conductor. The *x* and *y*-coordinates of this artificial boundary are usually few multiples of the transmission line height above the ground plane. In the literature[13-17], a technique called *ballooning* has been proposed to simulate this artificial boundary at infinity for electromagnetic field problems. Davis and Hoburg[6] adopted the ballooning technique for the solution of ionized field in conductor-to-plane configurations but did not report details of their finite-element ballooning formulation.

In the present paper, a new iterative finite-element ballooning technique (FEBT) is proposed as a numerical tool to solve Poisson's equation. In addition, the constancy of the conductor surface field at the corona onset value is implemented directly as a boundary condition into the proposed FEBT formulation. Moreover, an experimental set-up has been built to verify the results predicted by the proposed algorithm.

2. Mathematical Description of a Monopolar Ionized Field

The equations that constitute the mathematical description of the monopolar ionized field in air are:

$$\nabla.\vec{E} = \rho / \varepsilon_0 \tag{1}$$

$$\nabla.\vec{j} = 0. \tag{2}$$

$$\vec{J} = k \ \rho \ \vec{E} \tag{3}$$

$$\vec{E} = -\nabla\varphi \tag{4}$$

where ε_0 is the permittivity of free space *k* is the ion mobility.

Equations (1)-(4) are respectively, Poisson's equation, current continuity condition, the equation of current density and the equation relating the electric field to the potential.

These differential equations must be solved for the potential φ and the space-charge density ρ, both being functions of the space coordinates.

In reality, it is extremely difficult to find an exact solution to these equations due to their nonlinear nature. However, there are analytical solutions for simple geometries such as spherical and coaxial configurations[1,18]. All attempts for solving these differential equations were based on some simplifying assumptions[19-21]. The most common ones are:

(a) The thickness of the ionization layer around the conductor is so small to be disregarded with respect to the interelectrode spacing. The entire electrode spacing is filled with monopolar space-charge of the same polarity as the coronating conductor.

(b) The space-charge affects only the magnitude and not the direction of the electric field. This assumption was suggested at first by Deutsch and later on referred to as 'Deutsch's assumption'.

(c) The mobility of ions is constant (independent of field intensity),

(d) Diffusion of ions is neglected, and

(e) The surface field of the coronating conductor remains constant at the onset value E_0, which is known as Kaptzov's assumption[19] and before as Peek's assumption. For the conductor-to-plane configurations, E_0 is expressed in kV/m as[22]:

$$E_0 = 30 \ \eta(1+\sqrt{(9.06/R)}\times 10^{-2}) \tag{5}$$

where R is the conductor radius in cm and η is the surface irregularity (roughness) factor (= 1 for smooth conductors) and at a relative air density of 1.

3. Proposed Method of Analysis

In this paper, a new iterative finite-element ballooning technique is proposed to solve the ionized field problem in conductor-to-plane configurations without resort to Deutsch's assumption. In the following three subsections, the boundary conditions, simplifying assumptions and procedure of solution are explained.

3.1 Boundary Conditions

Solution of (1)-(4) which describe the space-charge ionized field requires the following boundary conditions :

(i) The potential on the coronating conductor is equal to the applied voltage as the voltage drop across the ionization layer is relatively very small.

(ii) The potential on the grounded plane is zero, and

(iii) The magnitude of the electric field at the surface of the coronating conductor is assumed to be constant at the onset value E_0,

(iv) The potential values of the nodes on the artificial boundary defining the FET bounded-region are updated and utilized in the finite-element formulation.

In order to investigate the impact of adopting the last boundary condition on the accuracy of the algorithms proposed before [8-10], the *Ballooning* technique by which the fictitious boundaries are extended to infinity is applied for the monopolar conductor-to-plane configurations as discussed in detail in section 3.3

3.2 Simplifying Assumptions

The monopolar ionized field equations are solved in conductor-to-plane configurations where assumption (b) (of the list given in section 2) is waived in a simple manner. The constancy of the electric field at the surface of the coronating conductor at its onset value, assumption (*e*), is replaced by the assumption that the electric field, E_{crit}, is assumed to be function of the applied voltage, i.e.

$$E_{crit} = E_0 f_1 (V/V_{0f}) \qquad (6-a)$$

where the function f_1 is assumed to have the following form[2]:

$$f_1 = 1.1339 - 0.1678\left(\frac{V}{V_{0f}}\right) + 0.03\left(\frac{V}{V_{0f}}\right)^2 \qquad (6-b)$$

where the voltage V_{0f} for a smooth conductor-to-plane configuration is given as:

$$V_{0f} = E_0 R \ \ln(2H/R), \ H \gg R \qquad (6-c)$$

3.3 Procedure

The investigated conductor-to-plane configuration has a conductor radius R and height H above the ground plane, Fig. (1). The proposed method of analysis is described in the following procedure, Fig. (2).

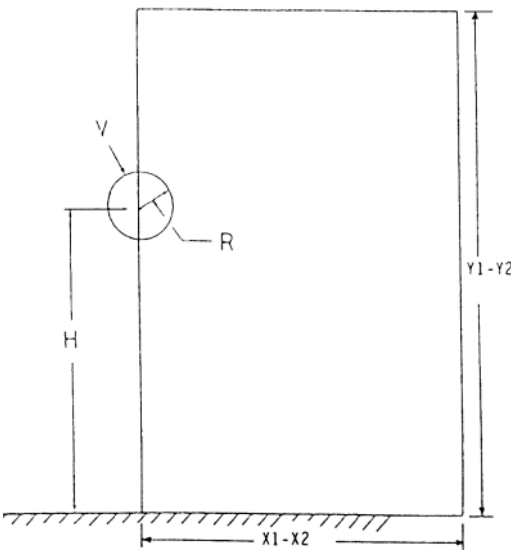

FIG. 1. Conductor-to-plane configuration.

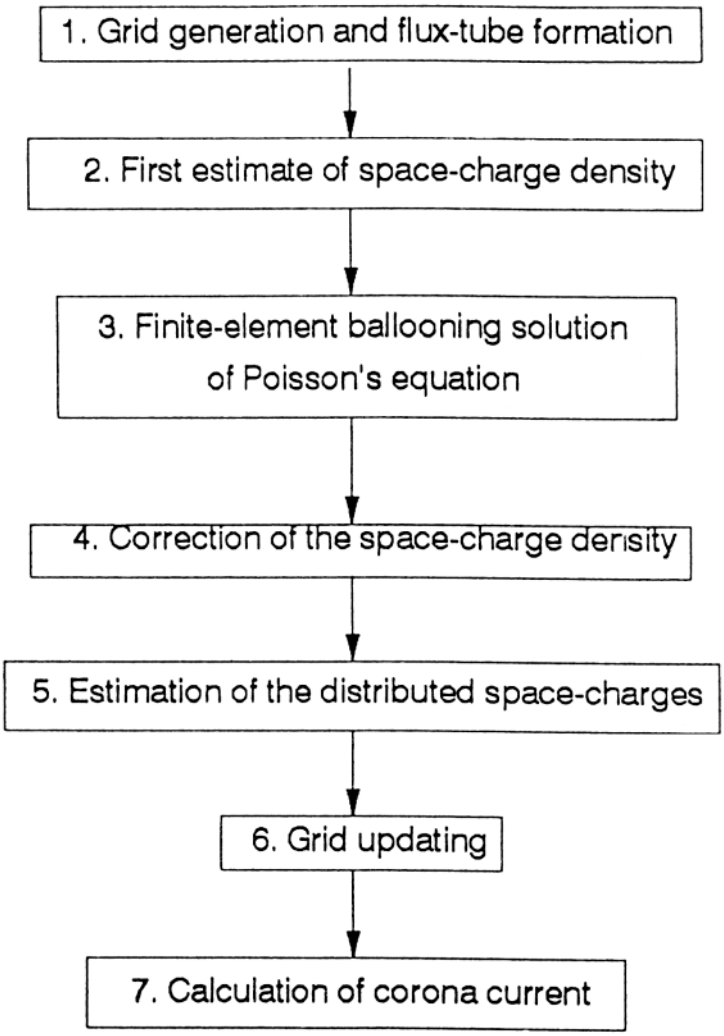

FIG. 2. Block diagram describing the proposed method of analysis.

Step (1): First Grid Generation and Flux-Tube Formation

The first grid is generated in the absence of space-charge and, therefore, the electric field is a space-charge free one due to the applied voltage *V*. To map the space-charge free field lines in the space, the conductor is simulated by a single-line charge displaced from its axis[9,23]. Due to symmetry about the Y-axis for the conductor-to-plane configuration, one half of the field lines is mapped where *M* nodes are selected on half of the circumference of the conductor forming the nodes from which the field lines emanate[9].

Therefore, the total number of field lines in the whole space is 2(*M*-1). The field is mapped in a region around the conductor which is defined by the fictitious boundaries X1-X2 and Y1-Y2 where X1-X2 and Y1-Y2 are located at 3.5-5.5 times the conductor height *H*, Fig. (1). This choice was found to be satisfactory in the light of the fact that the computed results did not change[9] for larger values of X1-X2 and Y1-Y2. In this paper, these fictitious boundaries are simulated at infinity as discussed in detail in section (5).

The total number of equipotential contours to be mapped is N. The conductor surface is equipotential at the applied voltage value and the ground plane is also equipotential at the zero value. Therefore, *N*-2 equipotential contours are traced in the interelectrode spacing, starting close to the conductor. Due to the fictitious boundaries X1-X2 and Y1-Y2, some of the field lines and equipotential contours will terminate at these boundaries.

The point of intersection between the i^{th} field line and the j^{th} equipotential contour represents the node (*i, j*) of the proposed grid for the conductor-to-plane configuration.

The potential $\varphi_{i,j}$ and electric field $E_{i,j}$ at each node (*i, j*), in the absence of space-charge, are denoted by $\Phi^{(1)}$ and $E^{(1)}$ i.e. the first estimate of potential and field values at nodes.

Step (2): First Estimate of the Space-Charge Density

For a first estimate of the space-charge density values at the proposed FE grid nodes, the space-charge density values are estimated by satisfying the continuity equation along each flux-tube. Simply, the continuity equation is satisfied by utilizing the fact that the current flowing in each flux-tube is constant.

The initial guess of the space-charge density located at node (*i,* 1) around the periphery of the coronating conductor is assumed[9] to follow eqn. (7).

$$\rho_{i,1} = \rho_e \cos((\theta_i)/2), \quad i = 1,2,3, \ldots M \tag{7}$$

where ρ_e is the value of $\rho_{i,1}$ at $\theta_i = 0$. The value of ρ_e was estimated[8] by eqn. (8)

$$\rho_e = \frac{E_g H}{E_0 R} 4\varepsilon_0 V_0 (V - V_0)/[H^2 V(5 - 4V_0/V)] \tag{8}$$

The corona onset voltage value V_0 is obtained from eqn. (9), as:

$$V_0 = R \; E_{crit} \; \ln \frac{2H}{R} \tag{9}$$

E_g is the space charge free electric field at the ground plane and
E_{crit} is determined from eqn. (6 - a).

As the current flowing in each flux-tube is constant along the tube[10], one can write the continuity equation for the i^{th} flux-tube as follows :

$$\rho_{i,1}E_{i,1}(A_{i,1})_n = \rho_{i,2}E_{i,2}(A_{i,2})_n = \rho_{i,N}E_{i,N}(A_{i,N})_n\,, \quad i = 1, 2, \cdots M \tag{10}$$

where the ion mobility is assumed constant.

In other words,

$$\rho_{i,j} = \rho_{i,1}\frac{E_{i,1}(A_{i,1})_n}{E_{i,j}(A_{i,j})_n},\ i = 1,2,\cdots M,\quad j = 1,2,\cdots N \tag{11}$$

where:

$(A_{i,j})_n$ is the per unit length cross-sectional area of the i^{th} flux-tube at the j^{th} equipotential contour along the direction normal to the electric field $E_{i,j}$, and

$E_{i,j}$ is the magnitude of the nodal field obtained in step (1).

Equation (11) gives the first estimate of the space-charge density at all nodes of the grid.

Step (3): Finite-Element Ballooning Solution of Poisson's Equation

The potential φ within each element is approximated as a linear function of coordinates[24], namely:

$$\varphi = \varphi^e W^e = \varphi_p w_b + \varphi_s w_s + \varphi_t w_t \tag{12}$$

with *p, s* and *t* represent the nodes of the element *e* and *W* is the corresponding shape function.

For known values of ρ at nodes, Poisson's equation is solved by minimizing an energy function with respect to each nodal potential value. This minimization leads to a set of simultaneous equations for values of φ at nodes. The array of nodal potentials is denoted by $\Phi^{(m)}$, representing the potentials in the m^{th} iteration.

The constancy of the conductor surface field at E_{crit} is implemented directly into the FE formulation. This is achieved by noting that $(\varphi_{i,1} - \varphi_{i,2})/\Delta r_i = E_{crit}$ where Δ_i is the radial distance between the first two nodes along the axis of any flux-tube,[9] and is much smaller than the radius of the coronating conductor. Since the potential $\varphi_{i,1}$ is the applied voltage which is known, then $\varphi_{i,2}$, the potential at node (*i*, 2), i.e. the i^{th} node along the second equipotential contour is also known.

Mathematical Formulation of the Ballooning Technique

Consider the monopolar conductor-to-plane transmission line configuration shown in Fig. (3). For the region *RI* with the boundary Γ_0, the FE global matrix equation can be formulated[24] as:

$$[S_{RI}][\Phi_{RI}] = \begin{bmatrix} S_{RR} & S_{R\Gamma_0} \\ S_{\Gamma_0 R} & S_{\Gamma_0\Gamma_0} \end{bmatrix}\begin{bmatrix} \Phi_R \\ \Phi_0 \end{bmatrix} = \begin{bmatrix} F_R \\ F_0 \end{bmatrix} \tag{13}$$

where

Φ_0	is the potential vector on the boundary Γ_0,
Φ_R	is the potential vector on the nodes of the interior region *RI*,
S_{RR}, $S_{I\Gamma 0 I\Gamma 0}$	are the self stiffness sub-matrixes in the interior region *RI* and on the boundary Γ_0, respectively.
$S_{I\Gamma 0R}$, $S_{RI\Gamma 0}$	are the mutual stiffness sub-matrices between the interior region *RI* and the boundary Γ_0, and
F_R, F_0	are the assembled free terms due to the boundary conditions.

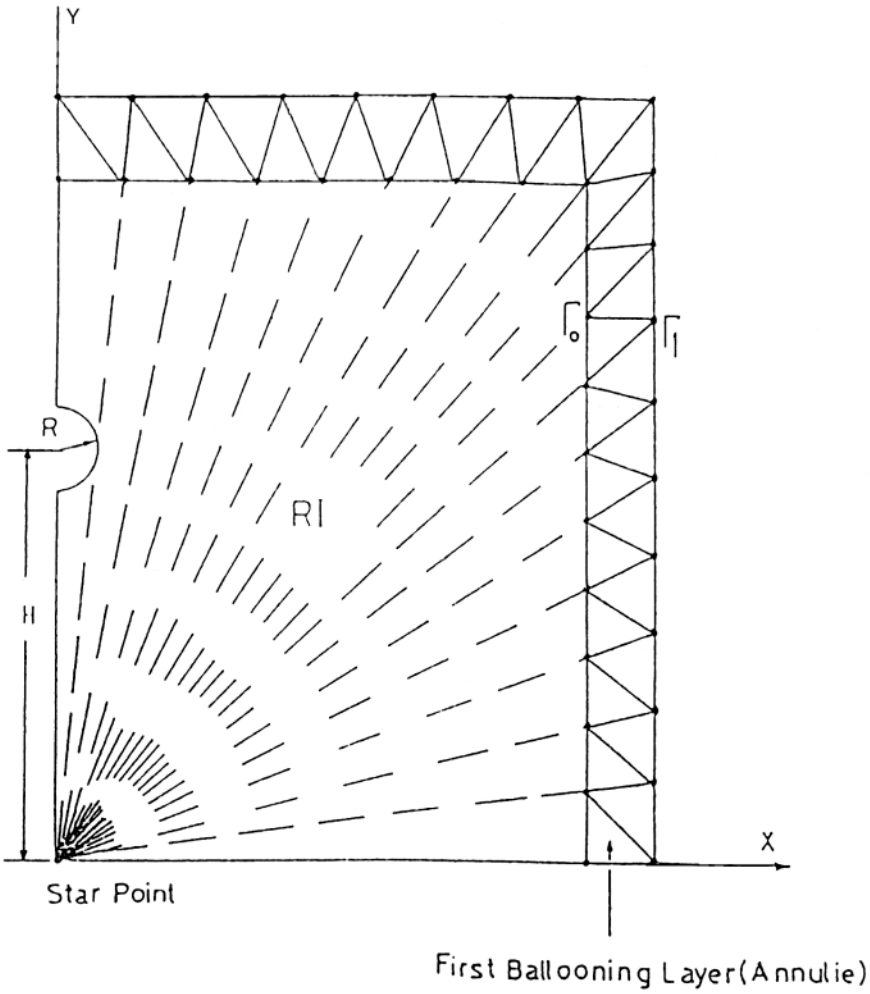

FIG. 3. The conductor-to-plane FE grid is bounded exterior region for the application of the ballooning technique.

Assume that the region exterior to *RI* contains only free space, hence the external field is purely Laplacian. The first step in the representation of the exterior region is to define a finite-element mesh for an *annular region* surrounding the region *RI*. This *annular region* has certain properties which can be summarized as follows:

(1) The number of nodes on the inner and outer boundaries are the same and lie on lines radiating from a star point, which is the point directly underneath the conductor at ground plane, Fig. (3).

(2) The outer boundary nodes for each successive ballooning annuals have a one-to-one correspondence with those nodes on the original boundary, Γ_0. This leads to useful geometric similarity properties applicable to the FE triangles in the ballooning region.

(3) There is a fixed mapping ratio α between the radii of the outer and inner sets of nodes of every annuals, measured from the star point.

Such an exterior annular region with boundary annuli Γ_0 , Γ_1 is shown in Fig. (4) around the fictitious boundaries X1-X2 and Y1-Y2.

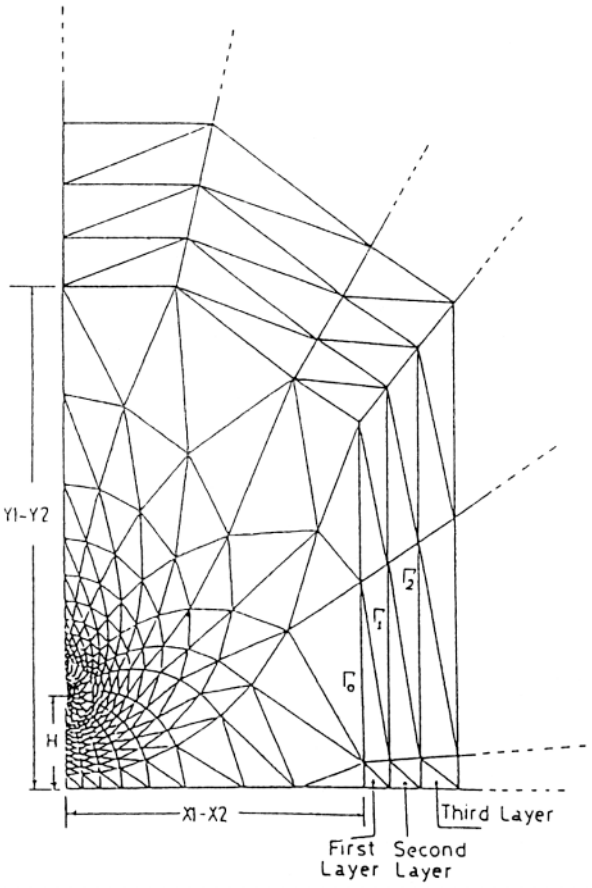

FIG. 4. Two-dimensional FE solution region with ballooning.

If the coordinates of the points on the inner boundary are denoted by $(x_n , y_n)^{(0)}$, then the coordinates of the outer boundary nodes are expressed as:

$$(x_n , y_n)^{(1)} = \alpha((x_n , y_n)^{(0)} \tag{14}$$

where α is the mapping ratio for the ballooning technique.

The FE matrix equation for nodes on Γ_0 , and Γ_1 is

$$S^1_{ext}\Phi^{0,1} = \begin{bmatrix} S^1_{11} & S^1_{12} \\ S^1_{21} & S^1_{22} \end{bmatrix} \begin{bmatrix} \Phi_0 \\ \Phi_1 \end{bmatrix} = \begin{bmatrix} 0 \\ 0 \end{bmatrix} \tag{15}$$

where S^1_{ext} is the stiffness matrix of the first ballooning layer (i.e. layer between the boundaries Γ_0 and Γ_1).

$$s^{(e)}_{ij} = \frac{\varepsilon_0}{4A_e}(q_i q_j + r_i r_j) \tag{16}$$

and *i, j = p, s, t,* the vertices of the element *e*, and

$$r_p = x_t - x_s , \quad r_s = x_p - x_t , \quad r_t = x_s - x_p$$

$$q_p = y_s - y_t , \quad q_s = y_t - y_p , \quad q_t = y_p - ys$$

and A_e is the area of the triangular element *e* expressed as

$$A_e = \frac{1}{2}[x_s y_t - x_t y_s + x_t y_p - x_p y_t + x_p y_s - x_s y_p] \tag{17}$$

In the same way, a second annuals for the nodes on Γ_1 , and Γ_2 can be constructed and the corresponding finite-element equation is expressed as:

$$T^1\Phi^{1,2} = \begin{bmatrix} T^1_{11} & T^1_{12} \\ T^1_{21} & T^1_{22} \end{bmatrix} \begin{bmatrix} \Phi_1 \\ \Phi_2 \end{bmatrix} = \begin{bmatrix} 0 \\ 0 \end{bmatrix} \tag{18}$$

where T^1 is the stiffness matrix of the second ballooning layer.

This second annuals is geometrically similar to the first and has the same mapping ratio, hence

$$(x_n , y_n)^{(2)} = \alpha(x_n , y_n)^{(1)} = \alpha^2(x_n , y_n)^{(0)} \tag{19}$$

Applying the geometric similarity given in equation (19) yields a set of elemental coefficients, $s^{(e)}_{ij}$, eqn. (17), which remains unchanged as one progresses from one ballooning annuals to the next. This means that the matrix T^1 in eqn. (18) is equal to the matrix S^1_{ext} in eqn. (16). That is, S^1_{ext} is identical to T^1, or

$$T^1 = S^1_{ext} \tag{20}$$

The two annuli can be combined to yield:

$$\begin{bmatrix} S_{11}^1 & S_{12}^1 & 0 \\ S_{21}^1 & S_{22}^1 + T_{11}^1 & T_{12}^1 \\ 0 & T_{21}^1 & T_{22}^1 \end{bmatrix} \begin{bmatrix} \Phi_0 \\ \Gamma_1 \\ \Phi 2 \end{bmatrix} = \begin{bmatrix} 0 \\ 0 \\ 0 \end{bmatrix} \tag{21}$$

where Φ_1 are the nodal potentials on the common boundary Γ_1, between the two annuli. The equations for Φ_0, Φ_1, and Φ_2 may be solved to eliminate Φ_1, using the fact that :

$$\Phi_1 = -(s_{22}^1 + T_{11}^1)^{-1} (s_{21}^1 \Phi_0 + T_{12}^1 \Phi_2) \tag{22}$$

substituting eqn. (22) into eqn. (21) yields:

$$S_{ext}^2 \, \Phi^{0,2} = \begin{bmatrix} S_{11}^1 - S_{12}^1 (S_{22}^1 + T_{11}^1)^{-1} & S_{21}^1 - S_{12}^1 (S_{22}^1 + T_{11}^1)^{-1} T_{12}^1 \\ -T_{21}^1 (S_{22}^1 + T_{11}^1)^{-1} S_{21}^1 & T_{22}^1 - T_{21}^1 (S_{22}^1 + T_{11}^1)^{-1} T_{12}^1 \end{bmatrix} \begin{bmatrix} \Phi_0 \\ \Phi_2 \end{bmatrix} = \begin{bmatrix} 0 \\ 0 \end{bmatrix} \tag{23}$$

Hence:

$$S_{ext}^2 = \begin{bmatrix} S_{11}^1 - S_{12}^1 (S_{22}^1 + T_{11}^1)^{-1} - S_{21}^1 & - S_{12}^1 (S_{22}^1 + T_{11}^1)^{-1} T_{12}^1 \\ -T_{21}^1 (S_{22}^1 + T_{11}^1)^{-1} S_{21}^1 & T_{22}^1 - T_{21}^1 (S_{22}^1 + T_{11}^1)^{-1} T_{12}^1 \end{bmatrix} = \begin{bmatrix} S_{11}^2 S_{12}^2 \\ S_{21}^2 S_{22}^2 \end{bmatrix} \tag{24}$$

The matrix equation of (23) has the same form of eqn. (16) but relates the two combined annuli, where the mapping ratio is α^2.

From the $(i-1)^{th}$ recursive ballooning step, applying the method given in eqn. (23) recursively, one could obtain:

$$S_{ext}^i \;\; \Phi^{0,i} = \begin{bmatrix} S_{11}^i & S_{12}^i \\ S_{21}^i & S_{22}^i \end{bmatrix} \begin{bmatrix} \Phi_0 \\ \Phi_i \end{bmatrix} = \begin{bmatrix} 0 \\ 0 \end{bmatrix} \tag{25}$$

which relates the potentials of the nodes on the boundaries Γ_0 and Γ_i.

For the i^{th} application, one can obtain in analogy with eqn. (18):

$$T^i \Phi^{i,i+1} = \begin{bmatrix} T_{11}^i & T_{12}^i \\ T_{21}^i & T_{22}^i \end{bmatrix} \begin{bmatrix} \Phi_i \\ \Phi_{i+1} \end{bmatrix} = \begin{bmatrix} 0 \\ 0 \end{bmatrix} \tag{26}$$

which relates the potentials of the nodes on the boundaries Γ_i and Γ_{i+1}.

Due to the geometric similarity property of the successive ballooning layers, we can write that:

$$T^i = S_{ext}^1 \tag{27}$$

Combining eqns. (25) and (26) and eliminating Φ_i, the following recursive relation for the ballooning technique can be written:

$$S_{ext}^{i+1} = \begin{bmatrix} S_{11}^i - S_{12}^i (S_{22}^i + T_{11}^i)^{-1} S_{21}^i & -S_{12}^i (S_{22}^i + T_{11}^i)^{-1} T_{12}^i \\ -T_{21}^i (S_{22}^i + T_{11}^i)^{-1} S_{21}^i & T_{22}^i - T_{21}^i (S_{22}^i + T_{11}^i)^{-i} T_{12}^i \end{bmatrix} = \begin{bmatrix} S_{11}^{i+1} S_{12}^{i+1} \\ S_{21}^{i+1} S_{22}^{i+1} \end{bmatrix} \tag{28}$$

It is quite clear that eqn. (24) is directly obtained from eqn. (28) when $i = 1$.

Hence, for the ballooned exterior region, we can write the following equation

$$S_{ext}^{i+1} \quad \boldsymbol{\Phi}^{0,\, i+1} = \begin{bmatrix} S_{11}^{i+1} & S_{12}^{i+1} \\ S_{21}^{i+1} & S_{22}^{i+1} \end{bmatrix} \begin{bmatrix} \boldsymbol{\Phi}_0 \\ \boldsymbol{\Phi}_{i+1} \end{bmatrix} = \begin{bmatrix} 0 \\ 0 \end{bmatrix} \tag{29}$$

Equation (29) relates the nodal potentials on the Γ_0 and Γ_{i+1} boundaries and has a mapping ratio of $\alpha^{(i+1)}$.

A new annular region can be added to the present outer nodes and the process can be repeated. Hence a recursive system has been defined with the outer boundary moving away with the following geometric progression:

$$\alpha^1, \alpha^2, \alpha^3, \cdots, \alpha^i \tag{30}$$

After m applications, one can write:

$$S_{ext}^{m} \quad \boldsymbol{\Phi}^{0,\, m} = \begin{bmatrix} S_{11}^{m} & S_{12}^{m} \\ S_{21}^{m} & S_{22}^{m} \end{bmatrix} \begin{bmatrix} \boldsymbol{\Phi}_0 \\ \boldsymbol{\Phi}_m \end{bmatrix} = \begin{bmatrix} 0 \\ 0 \end{bmatrix} \tag{31}$$

Finally, the S_{11} terms are attached to the outer modes of the interior solution region. That is, matrix eqn. (13) is combined with the matrix eqn. (31), yielding the following global finite-element system of equations:

$$\begin{bmatrix} S_{RR} & S_{R\Gamma_0} & 0 \\ S_{\Gamma_0 R} & S_{\Gamma_0 \Gamma_0} + S_{11}^m & S_{12}^m \\ 0 & S_{21}^m & S_{22}^m \end{bmatrix} \begin{bmatrix} \boldsymbol{\Phi}_R \\ \boldsymbol{\Phi}_0 \\ \boldsymbol{\Phi}_m \end{bmatrix} \begin{bmatrix} F_R \\ F_0 \\ 0 \end{bmatrix} \tag{32}$$

where:

$\boldsymbol{\Phi}_R$ is the vector of nodal potentials in the interior region *RI*,

$\boldsymbol{\Phi}_0$ is the vector of nodal potentials on the boundary Γ_0, and

$\boldsymbol{\Phi}_m$ is the vector of nodal potentials on the boundary Γ_m

If Γ_m is far enough, then $\boldsymbol{\Phi}_m$ approaches 0 and hence S_{21}^m approaches 0. Subsequently eqn. (32) becomes

$$\begin{bmatrix} S_{RR} & S_{R\Gamma_0} \\ S_{\Gamma_0 R} & S_{\Gamma_0 \Gamma_0} + S_{11}^m \end{bmatrix} \begin{bmatrix} \boldsymbol{\Phi}_R \\ \boldsymbol{\Phi}_0 \end{bmatrix} = \begin{bmatrix} F_R \\ F_0 \end{bmatrix} \tag{33}$$

In eqn. (32), as the number of ballooning layers (or annuli) increases, the coefficients of the matrix S_{12}^{m} converges (approaches) to zero.

Proposed Finite-Element Ballooning Algorithm

The steps of the proposed finite-element ballooning algorithm are as follows :

(1) Using the conventional FE technique, compute the global stiffness matrix S_{RI} (for the interior region) and the global stiffness F, eqn. (13).

(2) Choose a proper number of ballooning layers, m.

(3) Compute the matrix S_{ext}^{1}, eqns. (16) and (17).

(4) Set $i = 1$.

(5) Let $T^{i} = S_{ext}$.

(6) Use the main recursive relation (eqn. 28) to combine the matrix S_{ext}^{i} with T^{i} and obtain S_{ext}^{i+1}.

(7) If $i < m$, $i = i + 1$, go to (5).

(8) Incorporate the matrix S_{11}^{m} into the FE global matrix S_{RI} as in eqn. (33).

(9) Solve the FE equation given in eqn. (33).

(10) End the finite-element ballooning solution.

It is worthy to mention that the potentials estimated from eqn. (33) are $[\Phi_R]$ of the nodes in the interior region RI and $[\Phi_0]$ of the nodes on the boundary, Γ_0, located on the X1-X2 and Y1-Y2 boundaries. These estimated nodal potentials are expected to be more accurate than those estimated by previous attempts[8-10] since the FE ballooning algorithm extends his boundary to infinity. On the other hand, in previous attempts[8-10] the potential values at the nodes located on the X1-X2 and Y1-Y2 boundaries are estimated during the field mapping process.

Step (4): Correction of the Space-Charge Density

Comparing the last two estimates of the potential at the $(i, j)^{th}$ node $\varphi_{i,j}^{(1)}$ and $\varphi_{i,j}^{(l+1)}$, a nodal potential error e_n relative to the average value φ_{av} of the potential at that node is defined as

$$e_n = |\varphi_{i,j}^{(l)} - \varphi_{i,j}^{(l+1)}| / \varphi_{av} \tag{34}$$

where

$$\varphi_{av} = (\varphi_{i,j}^{(l)} + \varphi_{i,j}^{(l+1)})/2 \tag{35}$$

If the maximum of e_n along the axis of the i^{th} flux-tube exceeds a pre-specified value, δ_1, correction of the space-charge density values at the last node (corresponding to that i^{th} flux-tube) located either on the ground plane or on the Γ_0 boundary is made according to the maximum nodal error as in eqn. (36):

$$\rho_{i,N_{new}} = \rho_{i,N_{old}}[1 + g \max(\varphi_{i,j}^{(l+1)} - \varphi_{i,j}^{(l)})/\varphi_{av}] \ , \ \ i = 1, 2, \cdots M \tag{36}$$

where g is an accelerating factor, taken equal to 0.5. The error value δ_1 depends on the required accuracy (assumed 0.5% in the present paper).

The space-charge density at the other nodes along each flux-tube is corrected to keep the continuity condition of current satisfied, i.e.

$$\rho_{i,j} = \rho_{i,N} \frac{E_{i,N}(A_{i,N})_n}{E_{i,j}(A_{i,j})_n}\ ,\ i = 1,2,\ \cdots M,\ \ j = 2,3,\ \cdots N-1 \tag{37}$$

The space-charge density values at the conductor surface, $\rho_{i,1}$, $i = 1, 2, \cdots M$, are determined by extrapolation.

Step (5): Estimation of Discrete Space-Charges at Grid Nodes

The distributed space-charges are represented by discrete line charges extending parallel to the coronating conductor and located at the grid nodes. Hence, the charge per unit length at node (i, j) is:

$$Q_{i,j} = \rho_{i,j} v_{i,j} \tag{38}$$

where $v_{i,j}$ is the volume surrounding the node (i, j).

Step (6): Grid Updating

In the next grid generations, the traced field lines and equipotential contours are not only due to the applied voltage, but also due to the space-charges estimated at the grid nodes in step (5). Also, the recent space-charge density values around the periphery of the coronating conductors, $\rho_{i,1}$, $i = 1,2, \cdots M$ are the values obtained by the end of the last grid generation using eqn. (11).

Steps (1-6) are repeated until the maximum mismatch in the nodal space-charge density values between two successive grid generations is less than a pre-specified error δ_2 (assumed 0.5% in the present paper).

Step (7): Calculation of Corona Current

For each applied voltage above the onset value, the corona current is equal to the sum of the currents flowing in the $2(M-1)$ flux-tubes, i.e.

$$I = \sum_{i=1}^{2(M-1)} J_i A_{i,1} \tag{39}$$

As $J - k\rho E$, then

$$I = k[\rho_{1,1}E_{1,1}A_{1,1} + \rho_{M,1}E_{M,1}A_{M,1} + 2\sum_{i=2}^{M-1} \rho_{M,1}E_{M,1}A_{M,1}] \tag{40}$$

In eqn. (40), the first and second terms represent the current in the first and M^{th} flux-tube. The summation stands for the total current conducted in the remaining $M-2$ flux-tubes in the right or left half plane.

4. Experimental Set-Up and Procedure

Figure (5) shows a plan-view and a picture of the designed experimental arrangement which consists of

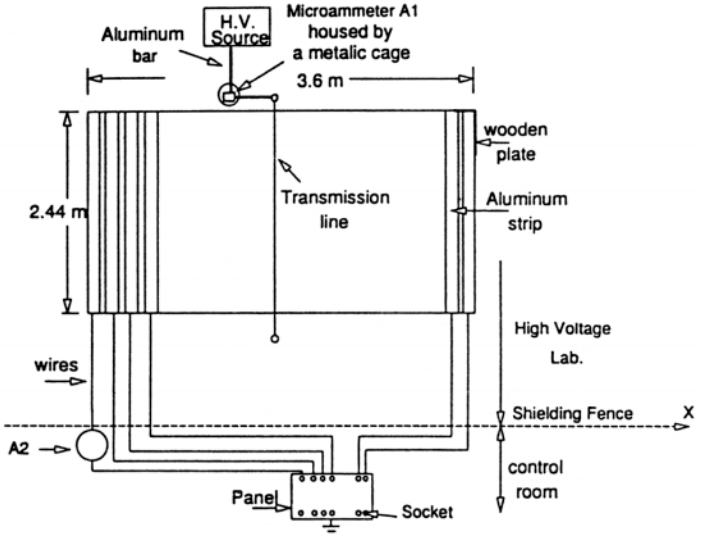

FIG. 5a. Experimental set-up: plan view.

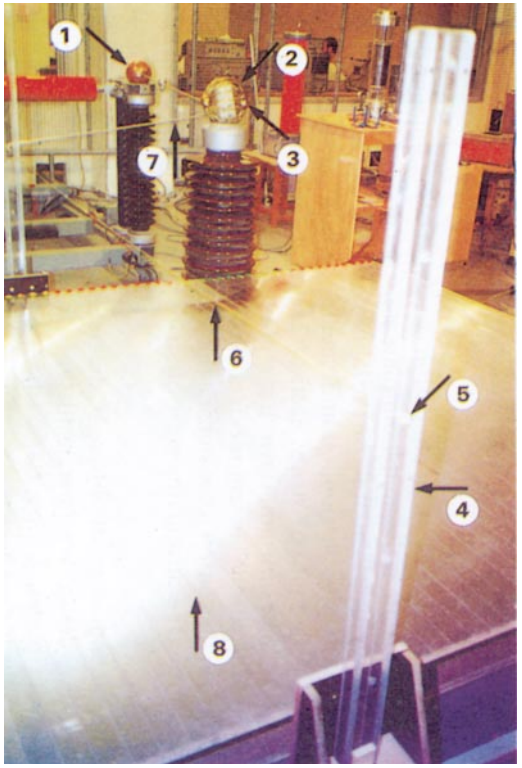

FIG. 5b. Picture at King Abdulaziz University high voltage laboratory.

1 – HV source	5 – Spherical cap
2 – Cage	6 – T.L. conductor
3 – Ammeter A 1	7 – Aluminum bar
4 – Isolating support	8 – Stripped aluminum plate

1) A grounded aluminum plate to simulate the ground-plane,
2) A conductor which represents the transmission line stretched between two isolating vertical supports,
3) A HVDC source to stress the line conductor, and
4) Two microammeters A1 and A2 for measuring the corona current and the ground-plane current density.

The grounded plate, $3.6 \times 2.44\ m^2$ in dimension, was made of aluminum sheet, 1 mm in thickness. To maintain the aluminum plate horizontally, it was fixed to a wooden plate of the same size at 0.50 m above the laboratory concrete floor. In order to measure the current density distribution underneath the transmission line, the aluminum plate was divided into 69 strips, each of $2.44 \times 0.05\ m^2$ and separated from each other by a distance of 1 mm. Each strip is grounded through the microammeter A2 to measure the corona current received by this strip. With the aid of the panel, Fig. (5), placed in the control room outside the laboratory, the microammeter A2 can serve in measuring the current flowing in all strips by switching it from strip to strip.

Transmission line conductors of different diameters (1.5 mm, 2.5 mm and 3.1 mm) are tested. In order to vary the transmission line height above the grounded plate, the height of the insulating supports was made variable. The two ends of the transmission line conductor are terminated by spherical caps in order to prevent corona from taking place at these ends.

To keep the HV current connection free from corona, the HV source is connected to the transmission line through microammeter A1 using a thick aluminum bar (10 mm diameter). As can be seen in Fig. (5), the microammeter A1 is housed in a spherical metallic cage to maintain it free from corona by preventing it from being exposed to the high electric field.

For a specified transmission-line configuration the applied voltage is increased gradually from zero and the reading of microammeter A1 is watched. When A1 starts reading, the applied voltage is the corona onset value. For different applied voltages above the corona onset value, the corona current is recorded to measure the V-I characteristics for this line configuration at different heights above the grounded plane.

For an applied voltage above the corona onset value, the current-density profile at the grounded plane is obtained by measuring the current changes from strip to strip on the grounded plate. Plots of the strip current-density versus the x-coordinate of the strip underneath the transmission line gives the required current-density profile.

5. Results and Discussion

The proposed method of analysis was applied to different laboratory models of conductor-to-plane transmission line configurations. The predicted values of the V-I characteristics and the current density profiles at the ground-plane for different configurations are discussed in the following sub-sections.

5.1 Comparison of the Present Calculated Values with those Reported before

5.1.1 V-I Characteristics

The proposed finite-element ballooning algorithm is applied to the monopolar conductor-to-plane transmission line configuration of[6,25]. The validity of the proposed algorithm is examined by comparing the calculated corona current and ground-plane current density values with those calculated[6] and measured[25] before.

The finite-element ballooning grid for the interior region and the first layer of the exterior region is shown in Fig. (4). The mapping ratio α is taken at 1.3[15,17] and the star point is directly underneath the conductor at the ground-plane, i.e. at $P(x_0, y_0)$ = (0, 0) as shown in Fig. (3).

When applying the proposed FE-ballooning algorithm, different ballooning layers (annuli) were used, i.e. m = 0, 3, 7, and 12. It was found that the improvement in the calculated values when using 12-ballooning layers over those obtained when using 7-layers is negligible.

Figure (6) shows the V-I characteristics (for a configuration H = 2m, R = 0.025 m, η = 0.942) obtained with ballooning layers (annuli), m = 0, 3 and 7, as compared to the characteristics obtained from experiment[25] and from previous attempt that adopted the ballooning technique[6]. It can be seen that assuming 0 layers introduced high error in the calculated V-I characteristics. For this configuration, comparison of the V-I characteristics obtained using previous algorithms[8-10] with those obtained experimentally[25] and numerically[6] is shown in Fig. (7). It is worthy to mention that for this transmission line configuration with 7 FE-ballooning layers, the computed results are in good agreement with the previously measured[25] and calculated values[6] as well as with the values calculated before by the authors[8-10]. Hence, one can conclude that imposing the artificial boundaries X1-X2 and Y1-Y2 around the transmission line conductors and evaluating the potential values at the nodes located on these boundaries for use in the FE formulation (as discussed in step (3) of section (3.3)) is appropriate. This conforms with the fourth boundary condition listed in section 3.1.

5.1.2 Current-density profiles at the ground plane

Figure (8) shows the calculated current-density profiles at the ground versus that obtained before[6,8-10] at 80 kV applied voltage. It is quite clear that the current density values obtained by the proposed method agree well with the previous experimental[25] than numerical[6,8-10] attempts. It is worthy to mention that the proposed algorithm predicts also the V-I characteristics and the current-density profiles at the ground-plane for full-scale transmission lines and the results agreed satisfactorily with experimental values[26].

5.2 Comparison of the Present Calculated and Measured Values

5.2.1 V-I Characteristics

Using the designed set-up, measurements were made for smooth (η =1) transmission lines conductors of different radii's and heights above the ground plane. For H = 0.29 m,

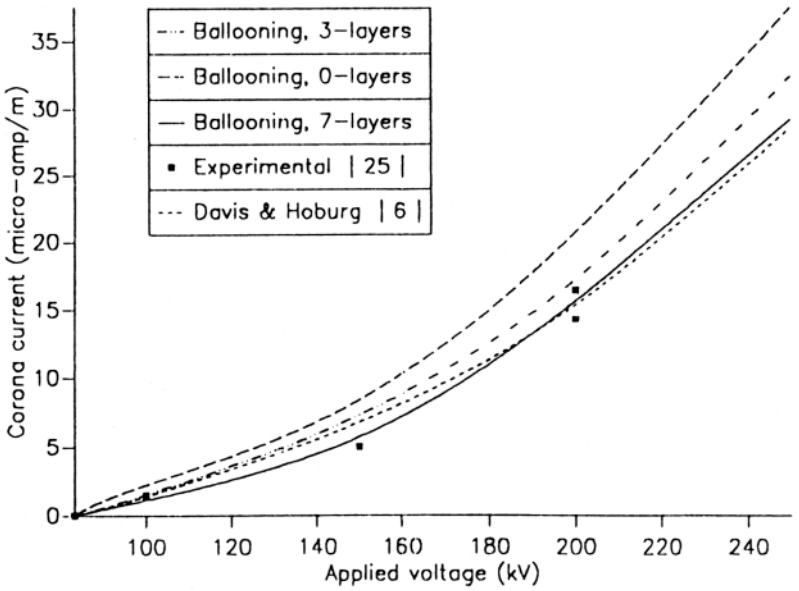

Fig. 6. Present calculated V-I characteristics of a laboratory conductor-to-plane configuration for different ballooning layers in comparison with those calculated and measured before (H = 2.0 m, R = 0.0025 m, η = 0.942).

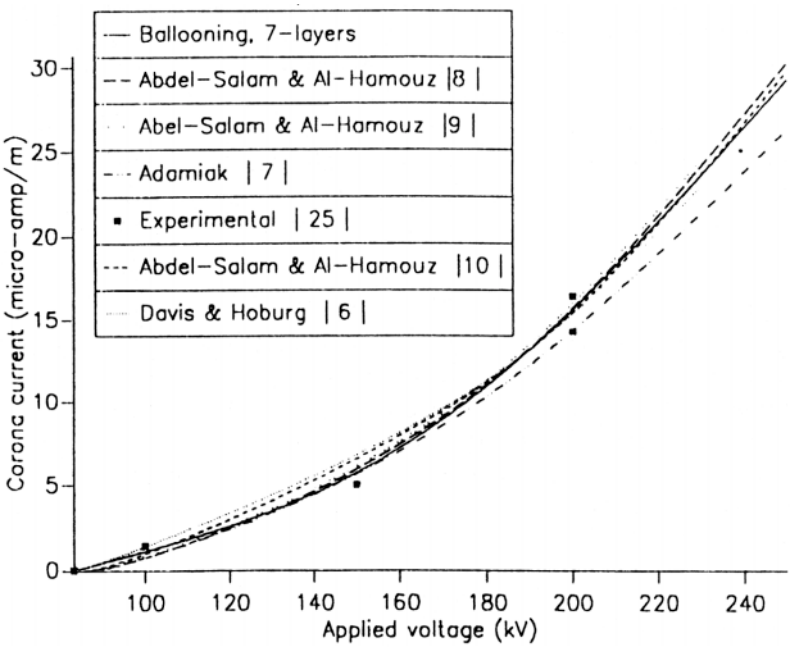

Fig. 7. Present calculated V-I characteristics of a laboratory conductor-to-plane configuration as compared with those calculated and measured before (H = 2.0 m, R = 0.0025 m, η = 0.942).

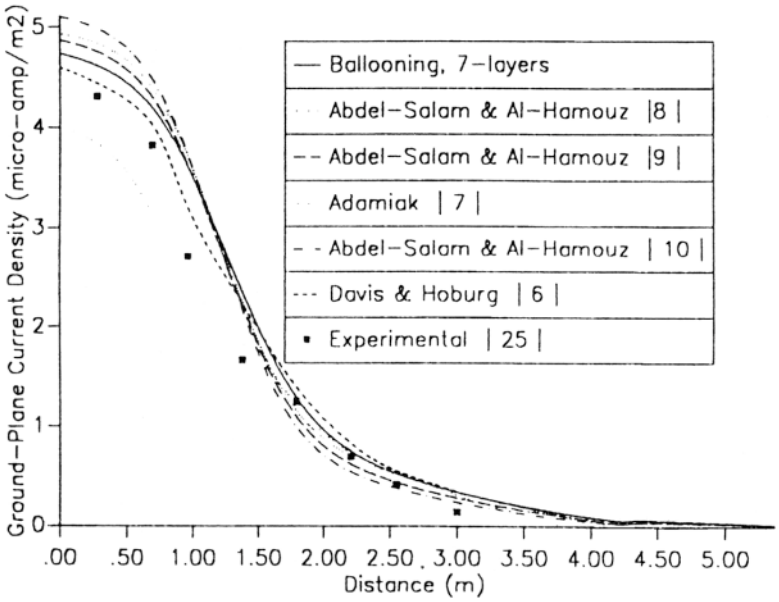

FIG. 8. Present calculated current density profile at the ground plane for a laboratory conductor-to-plane configuration in comparison with those calculated and measured before (V = 200 kV, H = 2.0 m, R = 0.0025 m, η = 0.942).

the present measured and calculated V-I characteristics are shown in Fig. (9) in comparison with the authors' previous attempts for two different conductor radii. It can be seen that the agreement between the present measured and calculated results is good. Also it can be seen that the FEBT algorithm predicts results that are in better agreement with the measured values than previous attempts.

For conductor radius of R = 0.75 mm the effect of varying the conductor height on the measured and calculated V-I characteristics is shown in Fig. (10). On the other hand, for the same conductor height above the ground plane, the effect of varying the conductor radius on the present measured and calculated V-I characteristics is shown in Fig. (11). It is quite clear that the agreement between the measured and calculated results is satisfactory.

5.2.2 Corona power loss

With the knowledge of the V-I characteristics for the transmission line configurations of Fig. (9), the corona power loss in kW/km is determined which increases nonlinearly with the applied voltage. It is worthy to mention that, when the line operates at its full capacity, the corona power loss as a percentage of the ohmic power loss is negligible (about 0.35%) when the applied voltage is very close to the corona onset value and reaches about 60% at an applied voltage of 1.8 times the onset value. Moreover, these percentages can assume higher values if the transmission line is lightly loaded[26].

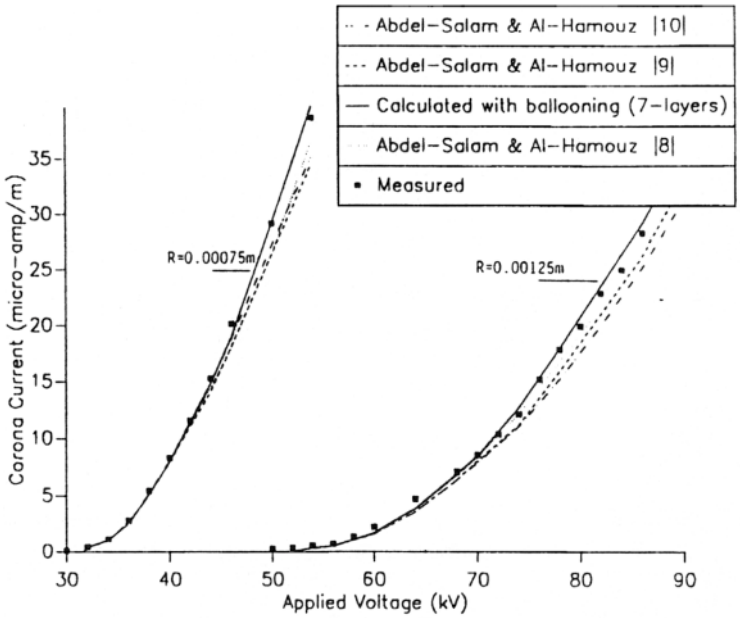

FIG. 9. Calculated and measured V-I characteristics of laboratory transmission-line configurations (H = 0.29 m, η = 1).

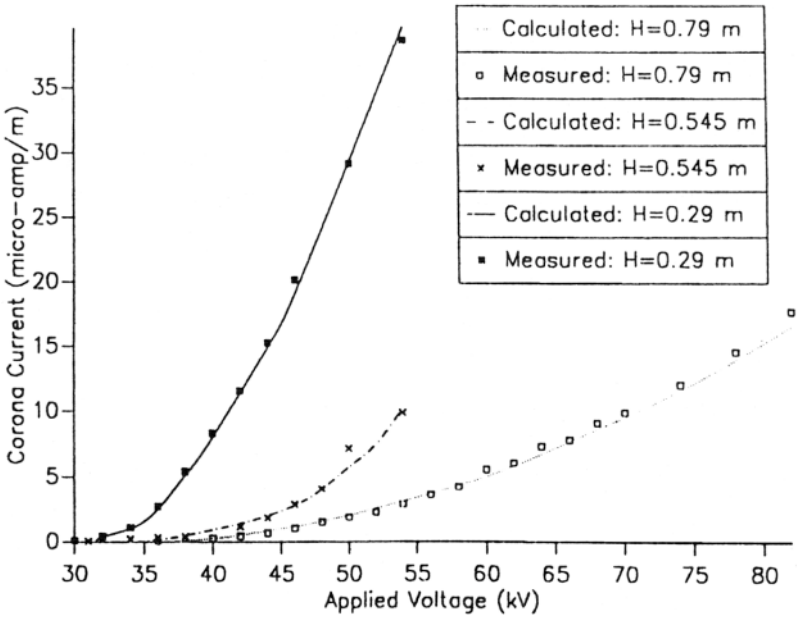

FIG. 10. Effect of conductor's height on the present measured and calculated V-I characteristics for a laboratory conductor-to-plane transmission line configuration (R = 0.00075 m, η = 1).

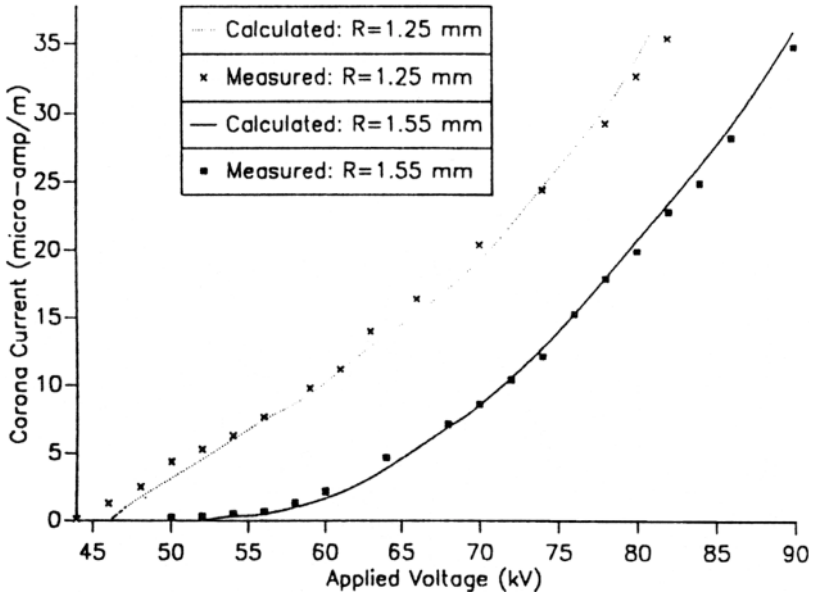

FIG. 11. Effect of conductor's radius on the present measured and calculated V-I characteristics for a laboratory conductor-to-plane transmission line configuration (H = 0.545 m, η = 1).

5.2.3 Current-density profiles at the ground-plane

For one of the transmission line configurations of Fig. (9), the measured and calculated ground plane current-density profiles at applied voltages of 54 kV and 82kV are shown in Fig. (12). It is clear that the agreement between the measured and calculated values is satisfactory. At the same time, it can be seen that the predicted results with ion diffusion are lower than those predicted by the ballooning algorithm. In addition, it can be seen that the measured current density profile is not completely symmetrical about the Y-axis. This can be attributed to some experimental errors.

5.3 Accuracy and simplicity of the proposed method

It is quite clear that the calculated values predicted by the proposed finite-element ballooning algorithm are in good agreement with the present measured and previously calculated values. On the other hand, it is worthy to mention that the values predicted by the FEBT are close to those measured by experiment, Figs. (7)-(9) and (12).

Also, it is worthy to mention that the results predicted when imposing the artificial boundary at 3.5-5.5 times the transmission line height, H, are close to those predicted when extending this artificial boundary to infinity (ballooning algorithm). Hence, one can conclude that imposing the artificial boundaries – as proposed in this paper – made it possible to approximately simulate the transmission line boundaries at infinity. Moreover, the proposed grid makes it easier to formulate the describing equations along the flux-tubes. All of this, of course, simplifies the proposed method of analysis.

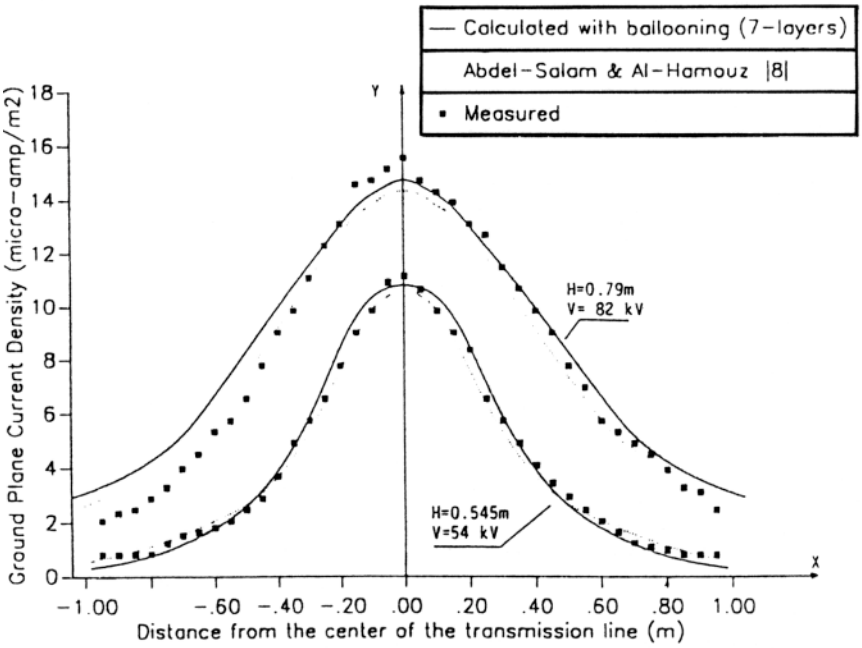

FIG. 12. Present measured and calculated current density profiles at the ground-plane as compared with the authors' previous calculation ($H = 0.545$ m, $R = 0.00075$ m, $\eta = 1$).

6. Conclusions

(1) An efficient iterative finite-element ballooning method has been developed for the analysis of ionized field in conductor-to-plane transmission line configurations. The proposed method simulates efficiently the commonly used artificial boundary around the transmission line at infinity.

(2) Unlike all attempts reported in the literature, the proposed finite-element ballooning technique implements directly the electric field at the coronating conductor as a boundary condition in the finite-element formulation.

(3) The agreement between the calculated values (corona current and current density profiles at the ground plane) and those measured by the authors and by others is satisfactory.

(4) Not only is the accuracy improved but also building the computer-program for the proposed method is simple.

Acknowledgments

The authors wish to thank their respective universities for the support they received during the progress of this work.

References

[1] **Abdel-Salam, M.,** *Electric Fields in High Voltage Engineering-Theory and Practice*, ed. Khalifa, M. (New York: Marcel Dekker), (1990).

[2] **Aboelsaad, M.M., Shafai, L.** and **Rashwan, M.,** Numerical assessment of unipolar corona ionised field quantities using the finite-element method, *IEE Proc., Pt.A,* **136:** 79-86, (1989).

[3] **Abdel-Salam, M.** and **Al-Hamouz, Z.,** A new finite-element analysis of an ionized field in coaxial cylindrical geometry, *J. Physics D: Appl. Phys.*, **25:** 1551-1555, (1992).

[4] **Takuma, T.** and **Kawamoto, T.,** A very stable calculation method for ion flow field of HVDC transmission lines, *IEEE Trans. Power Delivery*, **2:** 189-198, (1987).

[5] **Abdel-Salam, M., Farghally, M.** and **Abdel-Sattar, S.,** Finite element solution of monopolar corona equation, *IEEE Trans. Elect. Ins.*, **18:** 110-119, (1983).

[6] **Davis, J.L.** and **Hoburg, J.F.,** HVDC transmission line computations using finite element and characteristics methods, *J. Electrostat.*, **18:** 1-22, (1986).

[7] **Adamiak, K.,** Adaptive approach to finite element modelling of corona fields, *Proc. IEEE Ind. Appl. Society Annual Meeting, Houston, Texas, October 4-9*, (1992).

[8] **Abdel-Salam, M.** and **Al-Hamouz, Z.,** Analysis of monopolar ionized fields as influenced by ion diffusion, *Proc. IEEE-IA Annual Meeting, Toronto-Canada, 3-8 October 1993*, 1799-1804,, (1993).

[9] **Abdel-Salam, M.** and **Al-Hamouz, Z.,** Finite-element analysis of monopolar ionized fields including ion diffusion, *J. Physics D: Appl. Phys.*, 2202-2211, (1993).

[10] **Abdel-Salam, M.** and **Al-Hamouz, Z.,** Novel finite-element analysis of the space-charge modified field, *IEE Proc., Pt.A,* **141:** 369-378, (1994).

[11] **Ghione, G.** and **Graglia, R.,** Two-dimensional finite-boxes analysis of monopolar corona fields including ion diffusion, *IEEE Trans. Magnetics*, **26:** 567-570, (1990).

[12] **Levin, P.** and **Hoburg, J.,** Donor cell-finite element descriptions of wire-duct precipitator fields, charges and efficiencies, *IEEE Trans. Ind. Appl.*, **26:** 662-670, (1990).

[13] **Silvester, P.** and **Hsieh, M.,** Finite-element solution of 2-dimensional exterior-field problems, *IEE Proc.*, **118:** 1743-1747, (1971).

[14] **Silvester, P., Lowther, D., Carpenter, C.** and **Wyatt, E.,** Exterior finite element for 2-dimensional field problems with open boundaries, *IEE Proc.*, **124:** 1267-1270, (1977).

[15] **Csendes, Z.** and **Hamann, J.,** Surge arrester voltage distribution analysis by the finite-element method, *IEEE Trans. Power Appar. & Sys.*, **100:** 1806-1813, (1981).

[16] **Brauer, J.,** Open boundary finite elements for axisymmetric magnetic and skin effect problems, *J. Applied Physics*, **53:** 8366-8368, (1982).

[17] **Luo, Z.** and **Demerdash, N.,** A finite-element ballooning model for 2D eddy current open boundary problems for aerospace applications, *IEEE Trans. Mag.*, **101:** 803-811, (1992).

[18] **Spangenberg, K.R.,** *Vacuum Tubes* (New York: McGraw-Hill), (1948).

[19] **Kaptzov, N.A.,** *Elektricheskie Invlentiia v Gazakh i vakuumme* (Moscow: Ogiz), 587-630, (1947).

[20] **Sarma, M.P.** and **Janischewskyj, W.,** Analysis of corona losses on dc transmission lines Pt. I – Unipolar lines, *IEEE Trans. Power Appar. & Sys.*, **88:** 718-731, (1969).

[21] **Sarma, M.P.** and **Janischewskyj, W.,** Corona loss characteristics of practical HVDC transmission lines P. I – Unipolar lines, *IEEE Trans. Power Appar. & Sys.*, **89:** 860-867, (1970).

[22] **Horenstein, M.,** Computation of corona space charge, electric field, and V-I characteristics using equipotential charge shells, *IEEE Trans. Ind. Appl.*, **20:** 1607-1612, (1984).

[23] **Weeks, W.,** *Transmission and Distribution of Electrical Energy* (New York: Harper & Row), (1981).

[24] **Segerlind, L.,** *Applied Finite Element Analysis* (New York: John Wiley & Sons), (1984).

[25] **Hara, M., Hayashi, N., Shiotsuki, K.** and **Akazaki, M.,** Influence of wind and conductor potential on distributions of electric field and ion current density at ground level in DC high voltage line to plane geometry, *IEEE Trans. Power Appar. Sysm.*, **101:** 803-811, (1982).

[26] **Al-Hamouz, Z.,** *Analysis of the Ionized Field around HVDC Transmission Lines, Ph.D. Dissertation*, Dept. of Electrical Engineering, King Fahd University of Petroleum & Minerals, (1994) Dhahran, Saudi Arabia.

تحليـل انتفـاخي متكيف بطريقـة العنـاصر المحـددة لمجـال متـأين أحـادي القطبيـة

أنور حسن مفتي* ، زكريا الهموز و مازن عبد السلام****

** قسم الهندسة الكهربائية وهندسة الحاسبات ، كلية الهندسة ، جامعة الملك عبد العزيز جـــــدة – المملكة العربية السعودية*

*** قسم الهندسة الكهربائية ، كلية الهندسة ، جامعة الملك فهد للبترول والمعادن الظهـــران – المملكة العربية السعودية*

المستخلص . تقدم ورقة البحث أسلوبًا متكيفًا يستخدم العناصر المحددة لتحليل المجال المتأين أحادي القطبية في الأشكال ذات « الموصلات إلى الأرض » ، وذلك دون اللجوء إلى الاستعانة بافتراض « دويتسن » . وقد جرى اقتراح أسلوب انتفاخي تكراري جديد يستعمل العناصر المحددة في معادلة « بواسون » حيث تم عند اللانهاية محاكاة الحد الاصطناعي الشائع الاستخدام حول موصلات خط النقل . إن الأسلوب المقترح يسعى فقط إلى ايجاد حل لمعادلة تفاضلية جزئية ثنائية الرتبة بدلا من محاولة حل معادلة تفاضلية جزئية ثلاثية الرتبة وغير خطية أو محاولة حل معادلتين تفاضليتين جزئيتين آنيتين كلتاهما ثنائية الرتبة كما هو منشور في أدبيات الموضوع .

لقد اتفق التيار الهالي وكثافة التيار عند المستوى الأرضي المحسوبان ، اتفقا بصورة جيدة مع نظيريهما المقيسين في نموذج معملي . وتتميز الطريقة المقترحة بالدقة وبساطة البرمجة المحسابية .